MATERIALS SCIENCE

Unusual packing of soft-shelled nanocubes

Fang Lu[1]*, Thi Vo[2]*, Yugang Zhang[3]*, Alex Frenkel[2], Kevin G. Yager[1], Sanat Kumar[2†], Oleg Gang[1,2,4†]

Space-filling generally governs hard particle packing and the resulting phases and interparticle orientations. Contrastingly, hard-shaped nanoparticles with grafted soft-ligands pack differently since the energetically interacting soft-shell is amenable to nanoscale sculpturing. While the interplay between the shape and soft-shell can lead to unforeseen packing effects, little is known about the underlying physics. Here, using electron microscopy and small-angle x-ray scattering, we demonstrate that nanoscale cubes with soft, grafted DNA shells exhibit remarkable packing, distinguished by orientational symmetry breaking of cubes relative to the unit cell vectors. This zigzag arrangement occurs in flat body-centered tetragonal and body-centered cubic phases. We ascribe this unique arrangement to the interplay between shape and a spatially anisotropic shell resulting from preferential grafting of ligands to regions of high curvature. These observations reveal the decisive role played by shell-modulated anisotropy in nanoscale packing and suggest a plethora of new spatial organizations for molecularly decorated shaped nanoparticles.

INTRODUCTION

The packing of simple-shaped solid objects, e.g., cubes and spheres, into stable three-dimensional (3D) arrangements is relevant to important practical architectural problems going back to the Egyptian and Mayan pyramids and the Great Wall of China. Similarly, in medieval times, the problem of stacking cannonballs was of practical importance. The essential aspects of this class of problems date from the first known mathematical study by Aryabhatta on packing spheres in 499 AD, to Kepler's conjecture in the 17th century, and to its recent proof by Hales (*1*). While a packing of spheres in clusters (*2*, *3*) and condensed phases (*4*, *5*) and in mixtures (*6*, *7*) has attracted much attention in experimental studies, the shaped objects were typically considered for the mathematical problem of tiling space. However, recent progress in synthesizing nonspherical nano- and mesoparticles has spurred interests in revealing the 3D packing of anisotropic particles of various shapes (*8*–*11*).

Computational exploration of the anisotropic particles demonstrates that the interplay of particle shape and entropic effects can engender highly complex structures (*10*, *12*), from ordered to different degree of disordered structures. Unlike spheres, the relative orientation of shaped particles represents one of the unique characteristics of these organizations. For example, cubes and their truncated modifications were shown to exhibit a range of ordered and plastic phases (*13*–*17*). In particular, a governing principle emerges that neighbor particles contact closely and exhibit inherent interparticle orientations limited by the jamming rule (*9*, *18*, *19*), although the details of particle shape and rotational entropy were shown to diversify the final structure (*15*, *20*, *21*). Moreover, shape-shifting was used to investigate phase transformation between particles of different shapes, e.g., between cube and sphere (*14*, *22*) and between cube and octahedron (*23*).

In contrast, the assembly of anisotropic particles without such intimate contact can yield higher structural complexity since factors other than pure shape drive packing behavior (*24*, *25*). In particular, soft-shell capping can substantially modulate particle shape (*21*), affect interparticle interactions (*26*, *27*), and even dictate their anisotropic characteristics (*14*, *28*, *29*). Accordingly, the resulting packing substantially differs from that predicted for pure geometrical forms discussed to date (*16*, *30*, *31*). This scenario is usually not considered for macroscopic shapes, but, at the nanoscale, the particle synthesis is typically sculptured by ligands, and they are also used to manipulate particle binding properties. The ligands, typically chain-like molecules, provide a softness for the shaped particles. Moreover, recent computational studies show that ligands can provide spontaneous valence (*32*). Thus, understanding the behavior of these shaped objects with soft shells is of high importance for revealing principles governing nanoscale organizations.

In this study, we investigated the role of a soft shell, formed by grafted chains, on the packing of nanoscale cubes. The cube is the most basic polyhedral building block with surface termination of six identical crystallographic facets. The formation of 1D arrays with tunable cube orientations, i.e., either face to face or edge to edge, have been revealed in recent experiments of polymer-coated nanocubes (NCs) assembly, which depends on polymer chain length, rigidity, or grafting density (*28*, *29*, *33*). These observations further stimulate interest in assembling NCs into 3D structures.

Previous studies revealed that in the regime of thin shell (experimentally realized using short ligands), either simple cubic (SC) or rhombohedral structures have been observed in the assemblies of short ligand–coated NCs induced by solvent evaporation (*14*, *34*, *35*). The continuous phase transition from between those phases was also observed (*14*). Through delicately choosing solvent or by using truncated cubes in these evaporation-induced self-assembly processes, NCs can also be organized into body-centered tetragonal (BCT) structures with a corner-to-corner orientation (*30*, *36*). The regime of larger shells for cubes was investigated using DNA, and as a particularly versatile polymer, that provides ability to tune spacing and strength of interactions between nanoparticles (NPs). An application of the DNA-driven assembly (*37*–*40*) to the fabrication of 3D ordered arrays revealed in a recent study (*16*) that the NCs grafted with relatively rigid

[1]Center for Functional Nanomaterials, Energy & Photon Sciences Directorate, Brookhaven National Laboratory, Upton, NY 11973, USA. [2]Department of Chemical Engineering, Columbia University, New York, NY 10027, USA. [3]National Synchrotron Light Source II, Energy & Photon Sciences Directorate, Brookhaven National Laboratory, Upton, NY 11973, USA. [4]Department of Applied Physics and Applied Mathematics, Columbia University, New York, NY 10027, USA.
*These authors contributed equally to this work.
†Corresponding author. Email: sk2794@columbia.edu (S.K.); og2226@columbia.edu (O.G.)

DNA motifs form SC and corner-to-corner BCT lattices depending on the DNA length. These similarities with ligand systems indicate that both chain length and chain rigidity are defining contributors to the properties of shells and the formation of phases with specific translational and orientational orders (*30*, *36*, *41*). In the extreme case when DNA forms a relatively thick uniform shell, the cube shape can significantly be masked, leading to a random cube orientation and a formation of a plastic phase. Thus, despite a diversity of reported arrangements, characterized by lattice type and cube orientation in a unit cell, the previously observed well-defined phases have a common feature, a symmetry of cube orientation within a unit cell. In this scenario, an orientation of the cubes relatively to the vectors of the unit cell is the same for all three axes.

In this work, we reveal that for soft-shelled cubes, over a range of shells formed by grafted DNA chains, a new type of cube packing with broken orientational symmetry can occur. In that case, the orientation of cubes is the same with respect to only two vectors of a unit cell, while relative to the third axis, the orientation is different. This previously unknown cube packing within a lattice results in a peculiar, so-called zigzag (ZZ), arrangement. That orientation is adopted in both flat BCT and body-centered cubic (BCC) arrangements of NCs for medium and larger sizes of the soft DNA shells, formed by predominantly single-stranded (ss) motifs, while for shorter chains, a conventional SC packing with trivial symmetric orientation occurs. Our detailed theoretical modeling uncovers that the nontrivial NC orientations result from the anisotropic surface distribution of flexible DNA grafts, which allow reconciling conflicting requirements on coordination number for attraction (6) and repulsion (8) while still maintaining BCC and BCT crystal symmetry.

RESULTS

We first explored how a length of DNA chains affects the structure of shells formed around cubic NPs. We used gold (Au) NC with an average edge length of ~47 nm and corner curvature radius of ~8 nm (Fig. 1A; see Materials and Methods for the synthesis method). Soft DNA shells are created by grafting single-stranded DNA (ssDNA) chains (denoted as "linker") to the NCs through hybridization with oligonucleotides (denoted as "tether DNA") thiol anchored to the particle's surface. For these nanoscale objects, which exhibit a large variation in surface curvature, the local linker grafting density might depend on the chain length.

To probe this effect, we use small, 7-nm diameter, spherical Au NPs grafted with complementary DNA to serve as a "marker." The relative probability of binding the sphere at different locations on the NC surface (e.g., face versus edge versus corner) is a direct measure of the local DNA grafting density. We carried out the experiments for long DNA (N = 86, N refers to the total number of nucleotides per linker chain) and short DNA (N = 16) linkers on the NCs using scanning electron microscopy (SEM; Fig. 1B). Because of the top-view SEM projection, this experiment differentiates only two different marker locations, namely, face-or-edge versus edges-or-corner (Fig. 1C). On the basis of the analysis of about 200 tagged NC-NP clusters, we generated a histogram of the marker placements on the NC (Fig. 1, D_1 and D_2). We observed that, for the short linker, the majority of markers are at the face-or-edge locations (Fig. 1D_1), whereas, for long DNA, nearly equal amounts were found at the edge-or-corner and the face-or-edge locations (Fig. 1D_2). We model the preferential grafting of linker chains at locations of different curvatures on the NC surface by accounting for chain entropy at these different locations at the level of a mean-field approximation that is validated by more detailed atomistic simulations (see section S1 and fig. S8 for calculation details). Figure 1 (D_1 and D_2) shows agreement between theoretical predictions and experiments. Figure 1 (E_1 and E_2) then shows the theoretically derived probability distribution functions of grafting projected onto the corresponding locations on the NC surface

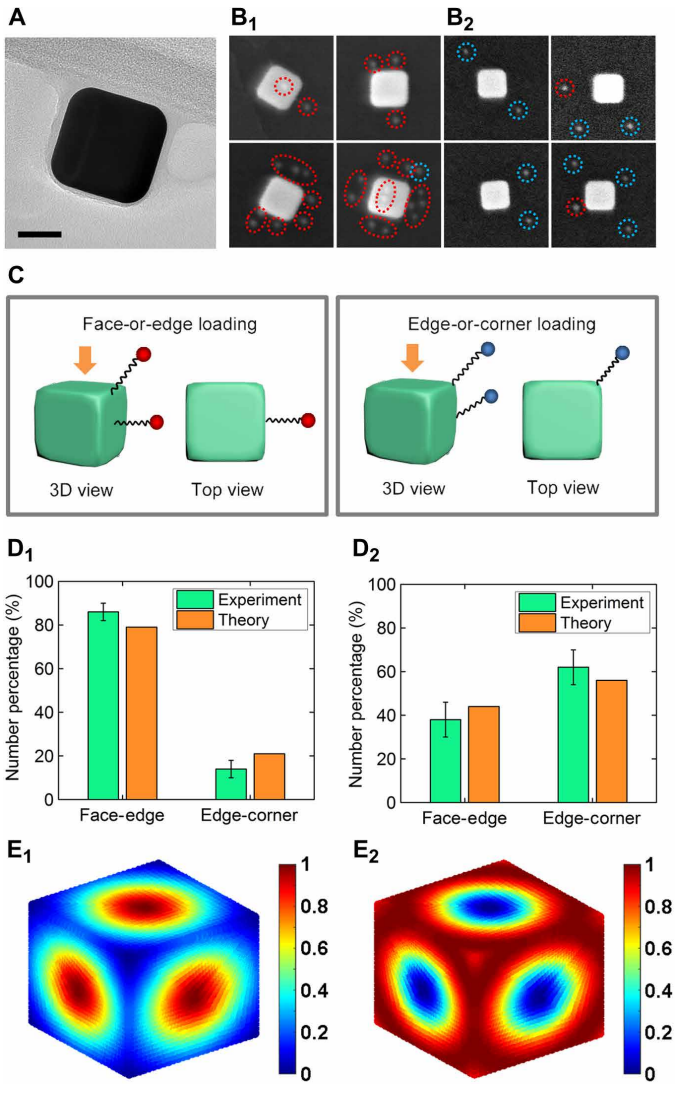

Fig. 1. Effect of chain length on DNA distribution upon cube surface. (**A**) A transmission electron microscopy image of gold (Au) NC. (**B_1** and **B_2**) Representative scanning electron microscopy (SEM) images of NC hybridized with spherical marker particles (small 7-nm Au NPs) using a short DNA linker (B_1, N = 16) and a long DNA linker (B_2, N = 86). N refers to the total number of nucleotides per linker chain. Binding site for marker particles in the representative SEM images is identified as face-or-edge and edge-or-corner, shown by dotted red and blue circles, respectively. (**C**) Definition of face-or-edge and edge-or-corner loading of marker in the top view. (**D_1** and **D_2**) Theory versus experimental comparison for preferential grafting as a function of linker chain length (D_1, N = 16; D_2, N = 86). (**E_1** and **E_2**) Probability distribution function of linker DNA grafting to various points on the surface of the cube (scale between 0 and 1) for short (E_1, N = 16) and long (E_2, N = 86) linker chains.

for short and long linkers, respectively. Here, the probability shown is relative to the point of least likelihood and scaled to range between 0 and 1. In agreement with the experiments, we predict a high attachment to the face-or-edge positions for $N = 16$ and a similar preference for the edge-or-corner relative to the face for the $N = 86$ system. These results imply that short chains prefer to graft on the faces, while longer chains preferentially bind to the high-curvature NC locations. We propose that this length-dependent distribution of linkers provides a facile means for modulating the shape of the DNA shell and, consequently, the ability to control cube-cube arrangements accompanying hybridization of their shells.

The DNA-driven assembly of NCs is a sensitive means to investigate the consequences of these chain length–dependent DNA shell shapes on NC packing. In the linker-induced NC hybridization system (denoted as LH), a binary set of NCs was generated by functionalizing NCs with either type A or B of noncomplementary single-stranded tether DNA (see Materials and Methods and table S1) (*42*). The tether DNA contains a 22-base spacer that separates an eight-base outer recognition segment from the NC surface. The ends of the ssDNA linker, L_M, are complementary to the respective ends of the tether DNA on the second NC population and are separated by a central flexible $(T)_M$ polythymine segment that contains M nucleotides ($M = N - 16$; see fig. S1). We formed each system (denoted accordingly as LH-M) by mixing an equal mole quantity of the two types of tether DNA–capped NCs and a linker L_M at a certain mole ratio of linker/cube A (or B). Following linker-driven assembly of NCs, we applied thermal annealing to achieve an equilibrium structural organization.

To fully establish the correlation between DNA shell shape and the NC arrangement in lattices, we investigated assembly behavior systematically by varying the linker length (M from 0 to 160). We used small-angle x-ray scattering (SAXS) to probe in situ the assemblies in the solution (fig. S2), which can give the symmetries, lattice constants, and particle orientation of a 3D structure. Modeling of NP superlattices has been performed to corroborate the structural results by comparing the model-derived SAXS patterns to the experimental ones. Scattering bands in Fig. 2A demonstrate three distinct chain length regimes signified by a splitting of the first peaks at LH-50 and a subsequent merging again at LH-85. With short linkers (L_0 to L_{40}), the NCs crystallize into an SC lattice, as confirmed by our SAXS simulation (Fig. 2A and fig. S2). This behavior is expected for cubes where face-to-face packing represents a closed-packed state. The position of the first peak in the structure factor $S(q)$, q_1, corresponds to the {100} crystalline plane in an SC lattice unit cell (see the scheme of Fig. $2B_1$). We found that, while the LH-30 reveals 12 orders of resolution-limited diffraction peaks in the corresponding $S(q)$, a peak broadening is observed for LH-40, which indicates decreased system order (fig. S2). Further, with a longer linker L_{50}, we observe a distinctly different scattering pattern as the first peak splits into two and q_1 shifts toward higher q. The system with linker L_{70} exhibits a typical scattering pattern of this second class of systems, wherein the scattering peaks index as a BCT lattice with a c/a ratio of 0.86 ($c < a = b$; see the scheme of Fig. $2B_2$). It is worth mentioning that, rather than a regular BCT lattice with a c axis longer than a ($c > a = b$), we obtain a flat BCT lattice with a c axis shorter than the other two in LH-50,

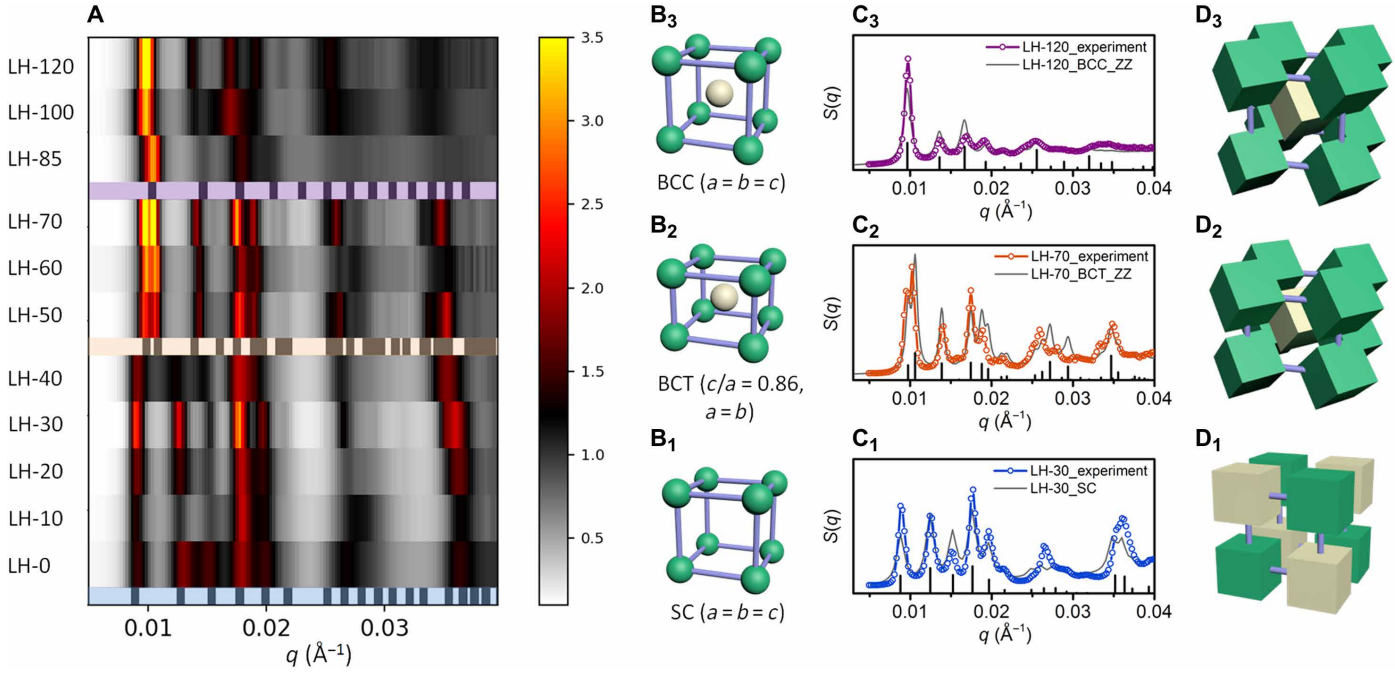

Fig. 2. The effect of linker DNA length on the cube assembly phase. (**A**) The evolution of the pattern for SAXS-measured structure factor $S(q)$ of the cube assemblies as a function of linker length. SC phase (blue region standard pattern) is observed from LH-0 to LH-40. BCT (orange region standard pattern) is observed from LH-50 to LH-70. BCC (purple-region standard pattern) is observed from LH-85 to LH-120. (**B_1** to **B_3**) The scheme of lattice for (B_1) SC-type, (B_2) flat BCT–type, and (B_3) BCC-type particle arrangement, which is coded with green and opal colors representing particles with noncomplementary DNA capping. (**C_1** to **C_3** and **D_1** to **D_3**) SAXS data with experimental (solid lines with markers) and modeled (gray solid line) $S(q)$ of (C_1) LH-30, revealing that the cubes crystallize into the SC lattice with a face-to-face orientation (scheme in D_1); (C_2) LH-70, revealing that the cubes crystallize into the flat BCT lattice with a ZZ orientation (scheme in D_2); and (C_3) LH-120, revealing that the cubes crystallize into the BCC lattice with a ZZ orientation (scheme in D_3).

LH-60, and LH-70. When the linker length increases further, there is another structural transition from an asymmetrical BCT crystal to a symmetrical BCC crystal, as observed in the cases of LH-85, LH-100, and LH-120 (see purple curve in Fig. 2A and the scheme of Fig. $2B_3$). Using an even longer linker L_{160} results in a disordered structure.

In the case of isotropic spheres as building blocks, positional order is the most important parameter for their assemblies, analogous to the atomic lattice systems (*37*, *38*, *43*). However, shape introduces more diversity to the assortment of 3D structures formed due to the orientation of anisotropic particles (*14*, *44*). To further investigate how linker length–dependent anisotropic DNA interactions accommodate NC arrangement in the lattices, we compared experimental and calculated SAXS patterns to determine cube orientations in the lattices (section S2). For example, for linker L_{30}, the scattering peaks are indexed as an SC lattice; the intensities of these peaks are best fit by a face-to-face orientation order of cubes with a DNA length of ~24 nm (Fig. $2C_1$). The cubes assembled with linker DNA ranging from L_0 to L_{40} behave analogously to the cubic hard core with 100% packing efficiency. In this case of face-to-face arrangement, DNA hybridizations would be maximized in a DNA length regime between 22 and 24 nm.

With intermediate linkers (L_{50} to L_{70}), where the NCs crystallize into flat BCT lattices, detailed analysis reveals the uniqueness of cube orientations. Typically, in the case of LH-70, the corresponding $S(q)$ does not match the models with either edge-to-edge, corner-to-corner arrangement or random orientations (plastic phase) of cubes (fig. S3). However, the model that includes a novel orientational ordering of cubes, namely, a ZZ-orientated BCT (ZZ-BCT; Figs. $2D_2$ and 3B), yields the best match with the experimental data. The cubes in such a ZZ-BCT structure have a special orientation (see fig. S4). For long linkers (L_{85} to L_{120}), the observed ZZ-BCC lattice can be achieved by implementing these operations on the BCC structure. A fixed native rectangular (*x*-*y*-*z*) coordinate system is based on a unit cell of BCC, wherein a rotation center is at the cube's center and three axes are normal to three faces of the cube, respectively. From the conventional corner-to-corner BCC arrangement, one can get the ZZ-BCC lattice by first rotating the cubes 45° around the *x* axis and then rotating them around the *z* axis by 45° (fig. S5). In the BCC lattice of cubes assembled with ZZ orientation, the manner where a cube hybridizes with its four nearest neighbors in the plane (110) is different from that in the plane (1-10) (fig. S6). The same rotating operations can also be applied to the cubes in the corner-to-corner BCT arrangement to obtain the ZZ-BCT lattice.

To visualize cube orientations in these lattices, we encapsulated the crystals in silica and characterized them with SEM (Fig. 3A). For short linkers (L_0), NCs are coordinated with their neighbors in a face-to-face manner, and crystalline grains exhibit a cubic Wulff shape (Fig. $3A_1$). The ZZ-BCT lattice assembled with linker L_{70} exhibits a different morphology: The grains appear approximately as rhombic dodecahedral (Fig. $3A_2$). Moreover, instead of a perfect face-to-face overlap, there is a clear shift between two neighbor cubes with faces partially matching, which meets with the cube packing pattern in the

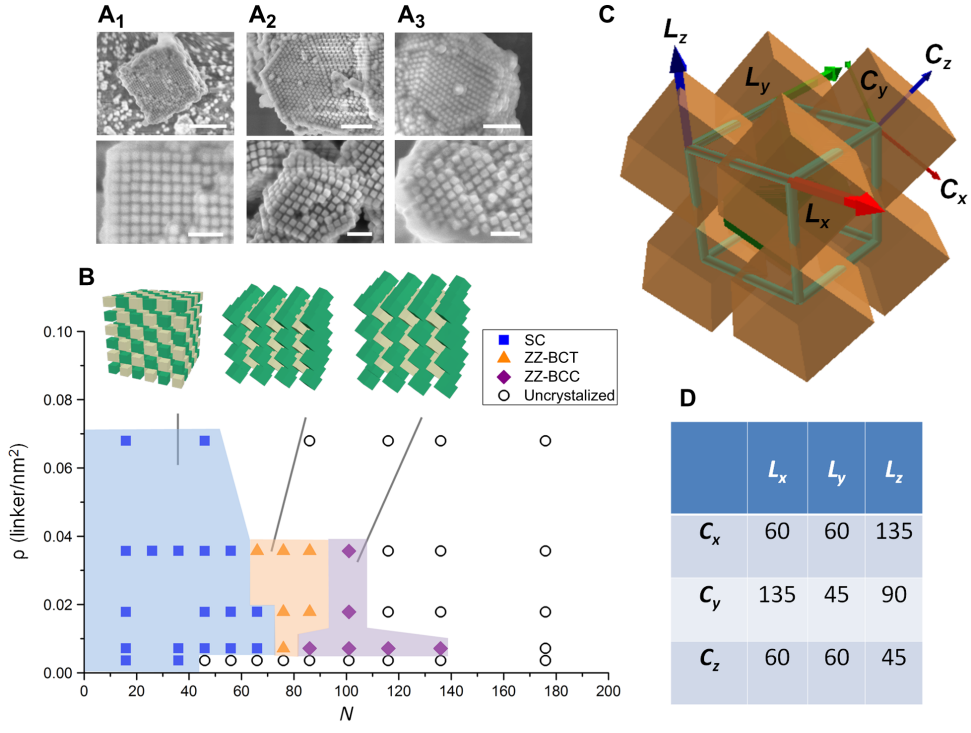

	L_x	L_y	L_z
C_x	60	60	135
C_y	135	45	90
C_z	60	60	45

Fig. 3. The assembly behavior of cubes as a function of DNA linker length and linker grafting density on the surface of cube. (**A_1** to **A_3**) Low (top cell)– and high (bottom cell)–magnification SEM images of silica-encapsulated lattices of (A_1) LH-30, (A_2) LH-70, and (A_3) LH-120. Scale bars, (A_1) 1 μm (top) 200 nm (bottom), and (A_2 and A_3) 500 nm (top) and 200 nm (bottom). (**B**) Phase diagram for cube-assembled lattices as a function of *N* (the nucleotides number per linker chain) and ρ (linker grafting density), coded with colors for different structures, *FF*-SC (blue), ZZ-BCT (orange), ZZ-BCC (purple), and disorder (white), as well as the corresponding structure schemes of {100}-enclosed cubic lattices. (**C**) Definition of lattice base vectors (L_x, L_y, L_z) and cube vectors (C_x, C_y, C_z) in a ZZ-BCC unit cell. (**D**) Table summarizes the angle between lattice base vectors and cube vectors, as defined in (C); a break of orientational symmetry of cubes in the ZZ-BCC and ZZ-BCT lattices is observed.

(110) plane of the BCT lattice (fig. S4). We also observe this feature of cube orientation in the solidified ZZ-BCC lattice assembled with linker L_{120} (Fig. 3A$_3$).

We obtain the morphology diagram for NC crystallization as a function of N (the nucleotide number per linker chain) and nominal grafting density of linker chain, ρ (Fig. 3B). At fixed ρ, a series of structural transitions occur accompanied by changes in the Bravais lattices as N increases, i.e., from a FF-SC crystalline phase to a ZZ-BCT and then a ZZ-BCC crystalline phase, followed by a transition to an amorphous phase. These ordered structures occur over larger ρ from smaller N values. For example, LH-0 (N = 16) exhibits an SC order for ρ from 0.0036 to 0.068, while LH-120 (N = 136) only forms a crystalline ZZ-BCC structure at ρ ~ 0.0071; LH-160 (N = 176) does not form a crystalline structure at all. These results indirectly imply that the number of available sites for linker attachment reduces with the length of linker chain. Further analyses of cube orientations in the ZZ structures reveal a break of orientational symmetry for both BCT and BCC lattices. As shown in the table of Fig. 3D, the angles between L_y and C_y and between L_z and C_z (45°) are the same, but the one between L_x and C_x (60°) is different (see figs. S6 and S7). On the contrary, in the previous studies (using either DNA, polymer, or surfactant decorations), an orientation of cubes was identical for all three directions (see section S3, figs. S9 to S11, and table S2) (*13*, *14*, *16*, *34*–*36*, *41*).

This unique break of an orientation symmetry is the result of the reconciliation of two conflicting coordination numbers: (i) The cubes with complementary strands have to maximize face-to-face interactions, determined by a coordination number of 6, but this is difficult to achieve in the BCC or BCT lattices, in which cubes have a coordination number 8; (ii) cubes with the same type of DNA strands have to minimize their repulsion, either through edge to edge or corner to corner, for both of which a coordination number is 8. Thus, a spontaneous break of orientational symmetry allows the system to satisfy this disparity in the "coordination" number of the different pairs of cubes while still maintaining those simple BCC and BCT lattices. In this ZZ phase, two faces of a central cube can hybridize with four faces of four complementary cubes (two cubes in the front and two at the back; Fig. 3C), while four other central cube's faces are hybridized with the remaining four cubes via face to face (two cubes on the left and two on the right sides; Fig. 3C). Note that this also allows the system to minimize repulsion between cubes with the same kind of DNA by orienting them either edge to edge or corner to corner. This unique organization is possible to accommodate due to the softness of the DNA shells, as we show below.

To further probe the effect of DNA corona shape on resulting cube assemblies, we first map out a complete set of corona morphology, which the DNA grafts can adopt within the range of relevant grafting density: That is, we do not consider the high-density regimes where we would trivially get a spherical corona. Our mean-field calculations based on the Daoud-Cotton model relevant to polymer brushes composed of long chains, which are verified by computer simulations at the chain lengths relevant to experiments, reveal three distinct corona shapes (Fig. 4A)—conformal or at (A$_1$), convex (A$_2$), and concave (A$_3$). These equilibrium results are understood as a competition between the translational entropy of the chains and the conformational entropy of the grafted chains. For short chains, where the chains do not have significant conformational entropy, the translational entropy wins and leads to a uniform grafting density across the cube—i.e., a conformal coating. For long chains and high grafting densities, however, conformational entropy wins and the chains preferentially graft at regions of the highest curvature, namely, the corners.

To gain insight into the corona shape as a driving force behind the morphology transitions, we perform a detailed calculation of the potential mean force (PMF) between a reference particle and its eight nearest neighbors (for a BCC face-to-face packing configuration). Here, we decouple the PMF into its attractive and repulsive components. Figure 4 (B$_1$ to B$_3$) shows the predicted particle packing orientations based on PMF calculations. The calculated lattices closely resemble the cube-cube packing orientation modeled in the SAXS form factor that provides for a good fitting of the calculated $S(q)$ to the experimental SAXS results. The convex corona morphology leads

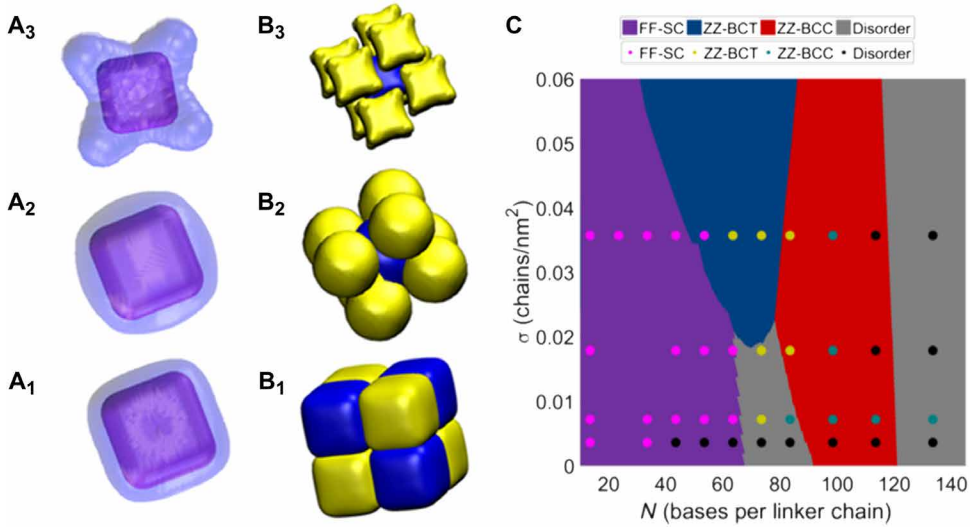

Fig. 4. Simulations reveal the mechanism behind the phase transitions of cube assemblies. (**A$_1$** to **A$_3$**) Simulated corona morphology transition as a function of grafting chain length: (A$_1$) conformal/flat, (A$_2$) convex, and (A$_3$) concave. Transitions occur for N = 40 and 80 for flat to convex and convex to concave, respectively. (**B$_1$** to **B$_3$**) Calculated particle packing orientations based on PMF calculations: (B$_1$) *FF*-SC, (B$_2$) ZZ-BCT, and (B$_3$) ZZ-BCC. (**C**) Phase diagram of predicted lattice as a function of chain length (N) and grafting density (σ); points correspond to the experimental data.

to the ZZ-BCT with a *c*/*a* ratio of ≈0.89; flat and concave coronas result in the SC and ZZ-BCC lattices, respectively. These two orientations for the SC and ZZ-BCC are identical to that predicted by the popular complementary contact model (CCM).

The results of our PMF analysis indicate that the repulsive interparticle interaction plays a major role in driving a reorganization of the particle packing orientation; while there are attractive DNA base-pairing interactions between the blue and yellow cubes in Fig. 4B, there are excluded volume (repulsive) interactions between the non-complementary DNA strands on two yellow (blue) cubes. The convexity of the corona shape creates extra overlap between neighboring particles (relative to the conformal coating), forcing a subsequent "shearing" and lattice expansion to offset the extra repulsions. However, this phenomenon cannot be captured by the current continuum contact model approaches, which to do not account for these orientational effects. To model these specific particle packing effects, we begin with the orientations predicted from our PMF analysis since this packing architecture optimizes attractive and repulsive interactions at the local graft-graft contact level; however, this does not capture longer range interactions. We use a Wertheim style first-order perturbation theory about a "hard-particle" crystalline reference state with the introduction of association sites on the surface of a particle to approximate the free energy (full details in section S4 and figs. S12 to S19). The transition to the perturbation theory allows for the explicit consideration of the individual orientation between neighboring particles and yields the calculated phase diagram (Fig. 4C). We note here that an additional advantage of the perturbation theory over the CCM is that we can also predict an order-disorder transition. In general, within a disordered state, clusters can exist from a single particle up to the maximum that is spatially allowed. To cast them in the framework of this model, we calculate the free energy for each cluster size using a liquid-state pair correlation function near the liquid-solid transition as the input structure and then Boltzmann average it across all possible cluster sizes for each given particle. The results, which are in excellent agreement with the experiment, not only emphasize the importance of corona morphology in controlling the self-assembled morphology but also highlight the need to explicitly consider asymmetric interactions to calculate the lattice free energy formation for anisotropic self-assembly. The formation of the ZZ-BCT can only be predicted by accounting for the difference in packing orientation between two particles relative to the other six particles within the lattice.

DISCUSSION

In summary, we have shown a novel orientational organization of cubic NPs with soft particle shells. Previous extensive computational studies did find that shape-shifting of solid cubes can produce such organization (*14*, *22*, *23*). This suggests a critical role of soft shells in promoting new types of organizations of self-assembled shaped particles. Our study reveals that cubic nano-objects demonstrate novel orientational order with a broken symmetry due to the ability of soft DNA shells to reconcile the conflicting requirements for a cube coordination number, as imposed by the details of intercube interactions. This work sheds light on the role of the soft shell in a formation of complex 3D organization of shaped objects and, consequently, on materials fabricated from anisotropic nano-objects. The DNA-offered capability to control nano-object separation distance, orientation, and lattice symmetry has important consequences for the rational design of nanomaterials.

MATERIALS AND METHODS

Synthesis of polyhedral gold NPs

Gold (III) chloride trihydrate ($HAuCl_4 \cdot 3H_2O$; 99.9+%), sodium borohydrate ($NaBH_4$; 99.99%), L-ascorbic acid (AA; 99.99%), cetyltrimethylammonium bromide (CTAB; 99.9%), and cetylpyridinium chloride (99%) were purchased from Sigma-Adrich and used without further purification. Milli-Q water with a resistivity greater than 18.0 megohm·cm was used in the preparation of aqueous solutions. Au nano-octahedral seeds were prepared using a modified two-step procedure (*45*). First, 3-nm Au seeds were prepared by quickly injecting 0.60 ml of ice-cold, freshly prepared $NaBH_4$ (10 mM) into a rapidly stirred mixture of $HAuCl_4$ (10 mM, 0.25 ml) and CTAB (0.1 M, 9.75 ml). The seed solution was stirred for 2 min and then left undisturbed at 25°C for 3 hours to ensure complete decomposition of $NaBH_4$ remaining in the solution. The seed solution was diluted 100 times with 0.1 M CTAB. For the synthesis of octahedral Au seeds, 4 ml of aqueous $HAuCl_4$ solution (0.3 mM), 24 ml of aqueous CTAB solution (20 mM), and 1.8 ml of aqueous AA solution (100 mM) were mixed, followed by adding 360 ml of the diluted seed solution under stirring. The mixture solution was then left to age at 25°C for 12 hours. In a typical synthesis of the Au NCs, 5 ml of the above 12-hour–aged seeds was first washed three times with 0.1 M CTAB solution using centrifugation (10,000 rpm for 10 min) and lastly condensed in 500 ml of 16 mM CTAB solution; 100 ml of 10 mM $HAuCl_4$ solution, 400 ml of freshly prepared 100 mM AA, and 500 ml of the condensed seed solution were added to 5 ml of 16 mM CTAB solution at 32°C consecutively and thoroughly mixed after each addition. The reaction was then left undisturbed for 6 hours and stopped by centrifugation (10,000 rpm for 10 min). The obtained NP solution was washed twice with Milli-Q water and concentrated for further usages. The synthesized Au NCs have an average edge length of ~46 nm, a size distribution of ~2%, and a yield of ~96%. The results were obtained from counting at least 200 NPs for each sample.

NP functionalization with DNA

Thiol-modified single-strand oligonucleotides (see table S1 for sequences) were purchased from Integrated DNA Technologies Inc. with disulfide modification. Before NP DNA functionalization, the disulfide oligonucleotides were first reduced by dissolving the lyophilized samples (100 to 300 nmol) in 0.3 ml of a 100 mM dithiothreitol solution in purified water or buffer. The reduced DNA was loaded on a freshly purified sephadex column (G-25, Amersham Biosciences) and eluted with 2.5 ml of 10 mM phosphate buffer (pH 7.4). The DNA was quantified using ultraviolet-visible (UV-vis) analysis using the known extinction coefficient. Au NPs were functionalized with ssDNA following a previously demonstrated method to achieve high DNA coverage (*46*). Briefly, an aliquot of purified DNA solution was added to 1 ml of aliquot of Au NPs (~3 optical density at 260 nm of DNA per milliliter of NP colloid). After allowing 1 to 3 hours for thiolated DNAs to react with the gold surface, particle suspensions were brought to 0.01% SDS and 10 mM sodium phosphate and allowed to sit for 1 hour. Following literature procedures, the colloidal NP solutions were then slowly treated with NaCl to allow for electrostatic screening between neighboring DNA strands and denser surface coverage of oligonucleotides. Specifically, the NaCl concentration of the solution was brought to 0.5 M slowly by adding aliquots of 3 M NaCl eight times with ~30-min interval for incubation. After reaching the final NaCl concentration, particles were allowed to sit overnight to achieve maximum DNA loading. To remove the

excess, unbound DNA from the solution, the mixture was centrifuged, the supernatant was removed, and the pellet was resuspended in washing buffer [0.01% SDS + 10 mM phosphate buffer (pH 7.4)]. This process was repeated three times. The final resuspension typically occurred in 50 to 100 ml to allow for a concentrated solution of particles in 0.2 M phosphate-buffered saline buffer [0.2 M NaCl + 10 mM phosphate buffer (pH 7.4)] for further assemblies. Concentration of NPs was quantified using the absorbance value at the surface plasmon resonance (SPR) maximum in UV-vis absorption spectra. A molar extinction coefficient of 3.5×10^{10} $M^{-1} \cdot cm^{-1}$ at the 546-nm SPR peak was used for the NCs with ~46-nm edge.

Assembly and crystallization of NP superlattices

The assembly was obtained by mixing equal molar amounts of type A and type B DNA-functionalized Au NCs, and a linker L*n* in a certain mole ratio of linker/type A (or B) DNA-functionalized NCs. The NCs were allowed to aggregate at room temperature. The samples were then annealed at a temperature ~3° to 5°C below the melting temperature of the assembled particles for a period of 30 min to several hours, depending on the sample. The annealed samples were transferred with buffer to a quartz capillary (1.0-mm diameter) and sealed with wax for SAXS measurements.

Characterization of NPs and assemblies

The morphology of NPs and the ex situ structure of assemblies were characterized using electron microscopy. Synchrotron-based SAXS (NSLS X9) was used to probe the in situ structure of particle assemblies.

UV-vis spectrophotometry

UV-vis spectra were recorded on a PerkinElmer Lambda 35 spectrometer (200 to 700 nm). Melting analysis was performed in conjunction with a PerkinElmer PTP-1 Peltier Temperature Programmer between 20° and 75°C with a temperature ramp of 1°C/min while stirring, in a 10 mM phosphate buffer, 0.2 M NaCl (pH 7.4), and buffer solution.

Scanning electron microscopy

SEM experiments were carried out on a Hitachi S-4800 scanning electron microscope with typical 1-kV voltage and 10-mA emission current. The sample was prepared by drop casting an aqueous NP solution on a cleaned silicon substrate.

Transmission electron microscopy

Transmission electron microscopy images were collected on a JEOL-1400 microscope operated at 120 kV. The samples were prepared by drop casting an aqueous NP solution on a carbon-coated copper grid.

Small-angle x-ray scattering

SAXS experiments were performed in situ at the X9 beamline at the National Synchrotron Light Source and the 11-BM Complex Materials Scattering (CMS) beamline at the National Synchrotron Light Source II (NSLS II). The scattering data were collected with a Dectris Pilatus 1 M and 2M pixel-array detectors, respectively, and converted to 1D scattering intensity versus wave vector transfer, $q = (4\pi/\lambda)\sin(\theta/2)$, where $\lambda = 0.9184$ Å and θ is the wavelength of incident x-ray beam and the full scattering angle, respectively. The data are presented as the structure factor $S(q)$, which was calculated as $Ia(q)/Ip(q)$, where $Ia(q)$ and $Ip(q)$ are background-corrected 1D scattering intensities extracted by angular averaging of detector images for a system under consideration and the corresponding unaggregated gold particles, respectively. The peak positions in $S(q)$ are determined by fitting to a Lorentzian function.

SEM and layer-by-layer sample preparation

The sample deposited on a cleaned silicon substrate was measured using a Hitachi S-4800 scanning electron microscope with typical 1-kV voltage and 10-μA emission current. A standard polyelectrolyte-assisted layer-by-layer method was applied to prepare the diluted NP-assembled clusters for SEM characterization (*44*). Silicon wafers were used as substrates for SEM characterization. The substrates were sonicated for 10 min in water and then in ethanol, subsequently thoroughly cleaned using piranha solution (H_2SO_4:H_2O_2, 7:3), rinsed with deionized water, and dried under an air stream. The wafers were stored in water until use. Before use, the wafers were first immersed in an aqueous solution of positively charged poly(diallydimethylammonium chloride) [PDDA; weight-average molecular weight (M_w) = 200,000, 1 mg/ml in 0.5 M NaCl aqueous solution] for 20 min, then in an aqueous solution of the polyanion poly(acrylic acid, sodium salt) (M_w = 15,000, 1 mg/ml in 0.5 M NaCl aqueous solution) for 10 min, and lastly, in PDDA solution for 10 min. At this stage, the wafers were positively charged, favoring the electrostatic interaction with negatively charged DNA in the assembled aggregates. To obtain a monolayer of NP-assembled clusters, the pretreated wafers were immersed in the corresponding solution with diluted aggregates and kept for a suitable period of time. After enough absorption, the substrates were rinsed with deionized water and dried under an air stream for further SEM characterization.

Theoretical modeling of NC coronas

To predict the corona shape about the NC cores, we took advantage of the polymeric behavior of ssDNA grafts and developed a scaling theory to quantify the free energy of grafts attached at various positions on the NC surface. This was carried out first by determining the free energy of chains grafted on an isotropic spherical surface and then performing a perturbation about the sphere to determine the excess energy associated at locations of different curvatures on the NC—namely, face, edge, or corner. The differences in the chain attachment free energies were then used in a Monte Carlo simulation to calculate the average distribution of grafts on the NC surface, from which the corona shape can be explicitly computed. Derivations of the scaling theory used to determine the chain free energy and simulation protocol are provided in the section S1.

Modeling of SAXS profiles for NC superlattices

To simulate powder SAXS profiles, we used our recently published scattering formalism, which simulates powder SAXS profiles for lattices of particles with arbitrary shape (*43*, *47*). This formalism accounts for particle size, particle shape, and particle orientation within the unit cell. We also explicitly included disorder: particle size polydispersity, lattice disorder (Debye-Waller factor), and average grain size. All SAXS modeling details are given in the section S2.

Lattice prediction using perturbation theory and effective DNA-NC coronas

To determine the effect of the corona shape on the self-assembled morphology, we developed a perturbation theory to compute the lattice free energy of formation for cubes with various corona shapes within the SC, ZZ-BCC, and ZZ-BCT morphologies. We first explicitly calculated the PMF between NCs with their effective attractive coronas at different relative orientations. These PMFs were then used to define the potential of interactions between neighboring particles in a preconstructed lattice to determine the excess energy of lattice formation

(relative to a purely repulsive "hard-corona" limit). The set of orientation, corona, and lattice that yielded the lowest free energy of formation was taken to be the thermodynamically stable structure. All theoretical derivations, simulation protocols, and algorithm development used to compute potential of interactions and lattice free energies between particles are provided in full detail in section S4.

SUPPLEMENTARY MATERIALS

Supplementary material for this article is available at http://advances.sciencemag.org/cgi/content/full/5/5/eaaw2399/DC1

Fig. S1. Schematics of particle-particle connections with linker DNA L_M.
Fig. S2. A full-set evolution of SAXS-measured structure factor $S(q)$ of cube assemblies with the linker length increasing (from LH-0 to LH-120).
Fig. S3. SAXS data with experimental and modeled structure factors $S(q)$ of LH-70 with different cube orientations in the BCT lattices.
Fig. S4. SEM image of the silica-encapsulated LH-70 lattice and the corresponding schemes.
Fig. S5. Schemes showing that the ZZ-BCC structure of cubes with a special orientation can be realized by rotating the cubes with a corner-to-corner orientation in the BCC lattice.
Fig. S6. Schemes of the ZZ-BCC structure composed of cubes and the projections viewed along various axes.
Fig. S7. Cubes exhibit a break of orientational symmetry in the ZZ lattices.
Fig. S8. Flat versus curved surface.
Fig. S9. Scheme and summary table of the angles between L_i and C_i ($i = x, y, z$) in a rhombohedral structure.
Fig. S10. Schemes and summary table of the angles between L_i and C_i ($i = x, y, z$) in SC or corner-to-corner BCT structures.
Fig. S11. Scheme and summary table of the angles between L_i and C_i ($i = x, y, z$) in the ZZ-BCT or BCC structure.
Fig. S12. Point-in-polygon calculations.
Fig. S13. Contour clustering.
Fig. S14. Clustering algorithm.
Fig. S15. Genetic algorithm for the traveling salesman problem.
Fig. S16. Traveling salesman problem for superellipsoid.
Fig. S17. Calculations for spherical overlap.
Fig. S18. Lattice free energy in the absence of any ligand grafting anisotropy.
Fig. S19. Phase diagram of corona morphology.
Table S1. DNA sequences used in the study.
Table S2. A summary table of the angles between L_i and C_i ($i = x, y, z$) in all previous studies.
Section S1. Theoretical modeling of NC shells (DNA coronas)
Section S2. Modeling of SAXS profiles for NC superlattices
Section S3. Comparison of cube's orientational symmetry and definition of a break of orientational symmetry of cubes
Section S4. Lattice prediction using perturbation theory and effective DNA-NC coronas

REFERENCES AND NOTES

1. T. C. Hales, Historical overview of the Kepler conjecture. *Discrete Comput. Geom.* **36**, 5–20 (2006).
2. V. N. Manoharan, M. T. Elsesser, D. J. Pine, Dense packing and symmetry in small clusters of microspheres. *Science* **301**, 483–487 (2003).
3. G. N. Meng, N. Arkus, M. P. Brenner, V. N. Manoharan, The free-energy landscape of clusters of attractive hard spheres. *Science* **327**, 560–563 (2010).
4. P. M. Chaikin, T. C. Lubensky, *Principles of Condensed Matter Physics* (Cambridge Univ. Press, 2000).
5. R. Zallen, *The Physics of Amorphous Solids* (Wiley, 1983).
6. E. V. Shevchenko, D. V. Talapin, N. A. Kotov, S. O'Brien, C. B. Murray, Structural diversity in binary nanoparticle superlattices. *Nature* **439**, 55–59 (2006).
7. D. V. Talapin, E. V. Shevchenko, M. I. Bodnarchuk, X. C. Ye, J. Chen, C. B. Murray, Quasicrystalline order in self-assembled binary nanoparticle superlattices. *Nature* **461**, 964–967 (2009).
8. P. F. Damasceno, M. Engel, S. C. Glotzer, Predictive self-assembly of polyhedra into complex structures. *Science* **337**, 453–457 (2012).
9. S. Torquato, Y. Jiao, Dense packings of the Platonic and Archimedean solids. *Nature* **460**, 876–879 (2009).
10. U. Agarwal, F. A. Escobedo, Mesophase behaviour of polyhedral particles. *Nat. Mater.* **10**, 230–235 (2011).
11. A. Donev, I. Cisse, D. Sachs, E. A. Variano, F. H. Stillinger, R. Connelly, S. Torquato, P. M. Chaikin, Improving the density of jammed disordered packings using ellipsoids. *Science* **303**, 990–993 (2004).
12. G. Soligno, M. Dijkstra, R. van Roij, Self-assembly of cubes into 2D hexagonal and honeycomb lattices by hexapolar capillary interactions. *Phys. Rev. Lett.* **116**, 258001 (2016).
13. L. Rossi, S. Sacanna, W. T. M. Irvine, P. M. Chaikin, D. J. Pine, A. P. Philipse, Cubic crystals from cubic colloids. *Soft Matter* **7**, 4139–4142 (2011).
14. Y. G. Zhang, F. Lu, D. van der Lelie, O. Gang, Continuous phase transformation in nanocube assemblies. *Phys. Rev. Lett.* **107**, 135701 (2011).
15. A. P. Gantapara, J. de Graaf, R. van Roij, M. Dijkstra, Phase diagram and structural diversity of a family of truncated cubes: Degenerate close-packed structures and vacancy-rich states. *Phys. Rev. Lett.* **111**, 015501 (2013).
16. M. N. O'Brien, M. Girard, H.-X. Lin, J. A. Millan, M. O. de la Cruz, B. Lee, C. A. Mirkin, Exploring the zone of anisotropy and broken symmetries in DNA-mediated nanoparticle crystallization. *Proc. Natl. Acad. Sci. U.S.A.* **113**, 10485–10490 (2016).
17. C. Knorowski, A. Travesset, Self-assembly and crystallization of hairy (*f*-star) and DNA-grafted nanocubes. *J. Am. Chem. Soc.* **136**, 653–659 (2014).
18. A. Haji-Akbari, M. Engel, A. S. Keys, X. Y. Zheng, R. G. Petschek, P. Palffy-Muhoray, S. C. Glotzer, Disordered, quasicrystalline and crystalline phases of densely packed tetrahedra. *Nature* **462**, 773–777 (2009).
19. L. Rossi, V. Soni, D. J. Ashton, D. J. Pine, A. P. Philipse, P. M. Chaikin, M. Dijkstra, S. Sacanna, W. T. M. Irvine, Shape-sensitive crystallization in colloidal superball fluids. *Proc. Natl. Acad. Sci. U.S.A.* **112**, 5286–5290 (2015).
20. K. Zhao, R. Bruinsma, T. G. Mason, Entropic crystal–crystal transitions of Brownian squares. *Proc. Natl. Acad. Sci. U.S.A.* **108**, 2684–2687 (2011).
21. M. A. Boles, D. V. Talapin, Self-assembly of tetrahedral CdSe nanocrystals: Effective "patchiness" via anisotropic steric interaction. *J. Am. Chem. Soc.* **136**, 5868–5871 (2014).
22. R. D. Batten, F. H. Stillinger, S. Torquato, Phase behavior of colloidal superballs: Shape interpolation from spheres to cubes. *Phys. Rev. E* **81**, 061105 (2010).
23. R. Ni, A. P. Gantapara, J. de Graaf, R. van Roij, M. Dijkstra, Phase diagram of colloidal hard superballs: From cubes via spheres to octahedra. *Soft Matter* **8**, 8826–8834 (2012).
24. Z. L. Zhang, S. C. Glotzer, Self-assembly of patchy particles. *Nano Lett.* **4**, 1407–1413 (2004).
25. J. Henzie, M. Grünwald, A. Widmer-Cooper, P. L. Geissler, P. Yang, Self-assembly of uniform polyhedral silver nanocrystals into densest packings and exotic superlattices. *Nat. Mater.* **11**, 131–137 (2012).
26. M. V. Kovalenko, M. Scheele, D. V. Talapin, Colloidal nanocrystals with molecular metal chalcogenide surface ligands. *Science* **324**, 1417–1420 (2009).
27. X. Ye, J. Chen, M. Engel, J. A. Millan, W. Li, L. Qi, G. Xing, J. E. Collins, C. R. Kagan, J. Li, S. C. Glotzer, C. B. Murray, Competition of shape and interaction patchiness for self-assembling nanoplates. *Nat. Chem.* **5**, 466–473 (2013).
28. A. Klinkova, H. Thérien-Aubin, A. Ahmed, D. Nykypanchuk, R. M. Choueiri, B. Gagnon, A. Muntyanu, O. Gale, G. C. Walker, E. Kumacheva, Structural and optical properties of self-assembled chains of plasmonic nanocubes. *Nano Lett.* **14**, 6314–6321 (2014).
29. B. Gao, G. Arya, A. R. Tao, Self-orienting nanocubes for the assembly of plasmonic nanojunctions. *Nat. Nanotechnol.* **7**, 433–437 (2012).
30. Z. Quan, H. Xu, C. Wang, X. Wen, Y. Wang, J. Zhu, R. Li, C. J. Sheehan, Z. Wang, D.-M. Smilgies, Z. Luo, J. Fang, Solvent-mediated self-assembly of nanocube superlattices. *J. Am. Chem. Soc.* **136**, 1352–1359 (2014).
31. M. C. Weidman, D. M. Smilgies, W. A. Tisdale, Kinetics of the self-assembly of nanocrystal superlattices measured by real-time in situ x-ray scattering. *Nat. Mater.* **15**, 775–781 (2016).
32. A. Travesset, Soft skyrmions, spontaneous valence and selection rules in nanoparticle superlattices. *ACS Nano* **11**, 5375–5382 (2017).
33. K. L. Gurunatha, S. Marvi, G. Arya, A. R. Tao, Computationally guided assembly of oriented nanocubes by modulating grafted polymer-surface interactions. *Nano Lett.* **15**, 7377–7382 (2015).
34. J. J. Choi, K. F. Bian, W. J. Baumgardner, D.-M. Smilgies, T. Hanrath, Interface-induced nucleation, orientational alignment and symmetry transformations in nanocube superlattices. *Nano Lett.* **12**, 4791–4798 (2012).
35. R. Li, K. Bian, Y. Wang, H. Xu, J. A. Hollingsworth, T. Hanrath, J. Fang, Z. Wang, An obtuse rhombohedral superlattice assembled by Pt nanocubes. *Nano Lett.* **15**, 6254–6260 (2015).
36. S. Disch, E. Wetterskog, R. P. Hermann, G. Salazar-Alvarez, P. Busch, T. Bruckel, L. Bergstrom, S. Kamali, Shape induced symmetry in self-assembled mesocrystals of iron oxide nanocubes. *Nano Lett.* **11**, 1651–1656 (2011).
37. D. Nykypanchuk, M. M. Maye, D. van der Lelie, O. Gang, DNA-guided crystallization of colloidal nanoparticles. *Nature* **451**, 549–552 (2008).
38. R. J. Macfarlane, B. Lee, M. R. Jones, N. Harris, G. C. Schatz, C. A. Mirkin, Nanoparticle superlattice engineering with DNA. *Science* **334**, 204–208 (2011).
39. M. Girard, J. A. Millan, M. O. de la Cruz, DNA-driven assembly: From polyhedral nanoparticles to proteins. *Annu. Rev. Mater. Res.* **47**, 33–49 (2017).
40. Y. Wang, I. C. Jenkins, J. T. McGinley, T. Sinno, J. C. Crocker, Colloidal crystals with diamond symmetry at optical lengthscales. *Nat. Commun.* **8**, 14173 (2017).
41. H. Chan, A. Demortiere, L. Vukovic, P. Král, C. Petit, Colloidal nanocube supercrystals stabilized by multipolar coulombic coupling. *ACS Nano* **6**, 4203–4213 (2012).
42. H. Xiong, D. van der Lelie, O. Gang, Phase behavior of nanoparticles assembled by DNA linkers. *Phys. Rev. Lett.* **102**, 015504 (2009).

43. Y. Zhang, F. Lu, K. G. Yager, D. van der Lelie, O. Gang, A general strategy for the DNA-mediated self-assembly of functional nanoparticles into heterogeneous systems. *Nat. Nanotechnol.* **8**, 865–872 (2013).
44. S. Vial, D. Nykypanchuk, K. G. Yager, A. V. Tkachenko, O. Gang, Linear mesostructures in DNA-nanorod self-assembly. *ACS Nano* **7**, 5437–5445 (2013).
45. F. Lu, K. G. Yager, Y. Zhang, H. Xin, O. Gang, Superlattices assembled through shape-induced directional binding. *Nat. Commun.* **6**, 6912 (2015).
46. M. R. Jones, R. J. Macfarlane, B. Lee, J. Zhang, K. L. Young, A. J. Senesi, C. A. Mirkin, DNA-nanoparticle superlattices formed from anisotropic building blocks. *Nat. Mater.* **9**, 913–917 (2010).
47. K. G. Yager, Y. Zhang, F. Lu, O. Gang, Periodic lattices of arbitrary nano-objects: Modeling and applications for self-assembled systems. *J. Appl. Crystallogr.* **47**, 118–129 (2014).

Acknowledgments
Funding: This research used resources of the Center for Functional Nanomaterials and the National Synchrotron Light Source II, which are U.S. Department of Energy (DOE) Office of Science Facilities at Brookhaven National Laboratory under contract DE-SC0012704. Research at Columbia University was supported by the DOE, Office of Basic Energy Sciences, Division of Materials Sciences and Engineering under grant DE-SC0008772. We thank Ruipeng Li and Masafumi Fukuto for their help with the NSLS II measurements. **Author contributions:** F.L., Y.Z., and O.G. initiated the concept. F.L. and O.G. designed the experiments. F.L. performed the experiments and analyzed the data. T.V. and S.K. conducted the theoretical and computational studies. A.F. contributed to the computational studies. Y.Z. and K.G.Y. performed the SAXS modeling and analysis. F.L., T.V., and O.G. wrote the paper. All authors edited the paper. S.K. supervised the computational part of the project. O.G. supervised and coordinated all aspects of the project. All authors discussed the results and commented on the manuscript. **Competing interests:** The authors declare that they have no competing interests. **Data and materials availability:** All data needed to evaluate the conclusions in the paper are present in the paper and/or the Supplementary Materials. Additional data related to this paper may be requested from the authors.

Submitted 30 November 2018
Accepted 11 April 2019
Published 17 May 2019
10.1126/sciadv.aaw2399

Citation: F. Lu, T. Vo, Y. Zhang, A. Frenkel, K. G. Yager, S. Kumar, O. Gang, Unusual packing of soft-shelled nanocubes. *Sci. Adv.* **5**, eaaw2399 (2019).